Relationship of flame propagation and combustion mode transition of end-gas based on pressure wave in confined space

Xiaojun Zhang[1], Haiqiao Wei[1,*], Xiaodong Cai[2], Ralf Deiterding[3], Lei Zhou[1,*]

1 State Key Laboratory of Engines, Tianjin University, Tianjin 300072, China

2 Science and Technology on Scramjet Laboratory, National University of Defense Technology, Changsha, 410073, China

3 Aerodynamics and Flight Mechanics Research Group, University of Southampton, Highfield Campus, Southampton SO171BJ, United Kingdom

*Corresponding author

Address: 92 Weijin Road, Nankai District, Tianjin, P. R. China

Tel.: +86-022-27402609

Email: lei.zhou@tju.edu.cn (L. Zhou)

      whq@tju.edu.cn

Abstract

The main objective of this work is to identify the end-gas combustion mode transition under different initial thermodynamics conditions and to focus on the role of pressure waves in autoignition formation and detonation development in the confined space by a group of two-dimensional (2D) numerical simulations with detailed chemistry of H_2/air mixture. Pressure waves with different strength are obtained by the flame acceleration in closed chambers with and without obstacles under three different initial temperatures. The results indicate that with the increase of initial temperature, there exist three different end-gas autoignition transition modes: no autoignition-autoignition transition, autoignition-no autoignition-autoignition transition and autoignition invariably. It is also shown that there three types of end-gas autoignition-induced detonation initiation: 1) detonation initiated directly by the pressure wave generated from the flame propagation; 2) detonation initiated directly by the pressure wave generated from other hot-spot autoignition; 3) autoignition to detonation transition based on the reactivity gradient theory. Meanwhile, to identify the autoignition transition

mode under continuous variation of pressure wave intensity and initial temperature, an idealized physical model, with the Mach number of the pressure wave as the link between the flame propagation duration and ignition delay time of the end-gas, is proposed. It is shown that the autoignition can be suppressed by the elevated flame speed when the pressure wave is weak, while it cannot be prevented intrinsically when the temperature of the end-gas is high or the pressure wave is strong enough. Moreover, different autoignition propagation modes are identified from Bradley's diagram, including deflagration, developing detonation and thermal explosion, and the combined effects of reactivity and pressure wave strength are discussed as well.

1. Introduction

Recently, many advanced combustion technologies have been proposed in internal combustion engines, motivated by further increasing the thermal efficiency and simultaneously achieving emission reduction, most of which have close association with the autoignition of fresh mixture [1-3]. On the one hand, the controlled autoignition can contribute to these novel combustion modes in compression ignition (CI) engines, such as homogeneous charge compression-ignition (HCCI) and low-temperature combustion (LTC) [2]. On the other hand, however, the unexpected autoignition can lead to knocking combustion in downsized and highly boosted spark ignition (SI) engines [3]. Two modes of knocking combustion, conventional knock and super-knock, are usually recognized. It is generally considered that conventional knock arises from autoignition (AI) of the end-gas ahead of the propagating flame, while the super-knock is induced by a local ignition prior to spark ignition, namely pre-ignition, followed by a violent autoignition and transition to detonation [3, 4]. Knock occurrence is usually accompanied by high-frequency pressure oscillation and the strong knocking combustion can cause destructive damage to the engines, which has become an obstacle for advanced engine design.

Despite the complexity of autoignition, in the past decades, considerable efforts have been undertaken in understanding its detail mechanism theoretically. As a pioneering work, Zel'dovich [5] proposed a classification for different autoignition propagation modes in the mixture with non-uniform reactivity. Later, Bradley and his coworkers [6-8] extended these studies and further developed an operational peninsula with two non-dimensional parameters as regime boundaries,

which can be adopted to classify different combustion regimes for a hot-spot. On the basis of above reactivity gradient theory, numerous experimental and numerical studies on autoignition modes, are conducted, because of its close relation to engine knock [9-13]. Pöschl et al. [14] investigated the effects of temperature inhomogeneity on autoignition development in an optical rapid compression and expansion machine (RCEM) and observed that a fast-propagating reaction front along the temperature gradient is induced by sequential autoignition, from which pressure waves are generated and consequently initiate a detonation. Cho et al. [15] studied the role of inhomogeneous fuel–air mixing on knocking characteristics and demonstrated that the lean spot is more reactive because of its higher temperature and can initiate knock while the rich spot cannot. Numerically, Liberman et al. [16] suggested that the evolution of spontaneous wave from the initial temperature gradient cannot be predicted by the one-step model quantitatively and qualitatively compared to the chain-branching kinetic model. Dai et al. [17] conducted a group of one dimensional (1D) simulations with hydrocarbon fuels and observed different autoignition modes caused by a cool spot with positive temperature gradient within the negative temperature coefficient (NTC) region. Zhang et al. [18] further investigated the detonation formation under concentration and temperature gradient numerically and pointed out that both concentration stratifications and its coupling with temperature gradient can have a significant effect on detonation initiation and combustion modes. Although these studies provide a deep understanding of the effects of reactivity gradient on autoignition modes, the initial inhomogeneity of mixture is artificially introduced and the early flame propagation in practical conditions is neglected as well as pressure wave evolutions, which is of great importance for formation of hot spots.

When the premixed flame propagates in the closed chamber, pressure waves are generated from it and continually compress the end-gas, which improves the temperature and pressure of the end-gas, benefiting for autoignition onset. Moreover, the coupling between pressure waves and the reaction front after autoignition onset may lead to detonation development and produce drastic pressure oscillation in the chamber [19, 20]. Therefore, pressure waves play a vital role in the autoignition formation and knocking combustion and have been extensively studied in the recent literatures experimentally and numerically. Using the optical RCM, Wang et al. [21] observed that the shock wave reflection at the wall initiates a detonation wave and they suggested that super-knock arises from the hotspot-induced deflagration to detonation transition followed by high-frequency pressure

oscillation. In order to obtain clear observations of the pressure wave evolution in the confined space, Wei et al. [22-25] conducted several experiments in a constant volume combustion chamber with Schlieren photography, wherein the shock wave formation and enhancement by the flame acceleration, as well as different combustion modes induced by the shock wave reflections, are all be captured. However, the complexity of the three-dimensional (3D) flow and limitations of measuring means make it difficult to reveal the underlying mechanism of autoignition induced by pressure wave reflections. Thus, some numerical simulations are performed to try to provide a deeper understanding of this process [26, 27]. Terashima et al. [28] investigated the effects of pressure wave on hot spot formation and showed that the periodic wall reflections of the compression wave lead to the production of a larger amount of chemical species compared to that of other end-gas points. Later, Terashima et al. [29] further demonstrated that different intensities of the pressure wave disturbance can induce different temperature inhomogeneities in the end-gas region and consequently lead to different end-gas autoignition behaviors. All these studies have significantly improved our understanding of the interactions among the flame, pressure waves and autoignition, three key elements in knocking combustion. Furthermore, there are a few studies focused on the competition of flame propagation and end-gas autoignition, which may provide a guide to knock suppression. Livengood and Wu [30] presented an integral method to predict the end-gas autoignition occurrence, based on which it is believed that engine knock can be suppressed by increasing the flame speed. In addition, Yu et al. [31] demonstrated that faster flame propagation and smaller chamber length can promote autoignition to no autoignition transition by 1D simulations. Also, Chen et al. [32] found that increasing the turbulence intensity and thus improving the flame speed can prevent knock in 3D simulations. However, the role of pressure waves is not emphasized in all these studies.

With above considerations, the present study aims to identify end-gas combustion mode transition under different initial thermodynamics conditions and to focus on the role of pressure waves in this process by a group of two-dimensional (2D) numerical simulations with detailed chemistry of H_2/air mixture. The new contributions of the present work are: 1) The obstacles adopted can realize different flame propagation speeds and controlled pressure wave intensities but cannot directly influence the ignition delay time of the end-gas, so that the relationships of flame propagation, pressure wave and autoignition can be clearly identified. 2) Different end-gas autoignition transition modes are observed, and an idealized model based on pressure wave intensity is proposed to

investigate the underlying mechanism for the first time to our best knowledge; 3) Different autoignition propagation modes are captured and the combined effects of pressure waves and initial thermodynamics are comprehensively analyzed. It should be noted that the previously mentioned "combustion mode transition" includes three aspects of understanding: The first is the autoignition transition mode, which means whether or not autoignition occurs in the end-gas. The second is the autoignition propagation mode, which means the reaction front propagates as deflagration, detonation or thermal explosion after autoignition occurrence. The third is the end-gas combustion at constant pressure or volume, which is actually directly relevant for the last mode. The present work will give deep insight into the mechanism of end-gas autoignition and knocking combustion.

The paper is organized as follows: the computational configurations and numerical methods are briefly discussed in Section 2. The results obtained by numerical simulations under different initial temperatures are separately shown in Section 3. Discussions on autoignition transition modes and autoignition propagation modes based on an idealized model and Bradley's diagram, respectively, are presented in Section 4. Finally, major conclusions from this work are summarized in the last section.

2. Computational configurations and numerical methods

2.1 Computational configurations

A set of 2D closed rectangular channels with and without obstacles are considered in the present work, whose length and height are denoted as $l = 2$ cm and $d/2 = 0.1$ cm respectively. The model with obstacles is schematically shown in Fig. 1. An array of uniformly spaced obstacles is placed at the upper wall. The thickness of the obstacles is 0.005 cm and the height 0.067 cm, which gives the blockage ratio of 0.67. The first obstacle starts at $X = 0.1$ cm and the distance between two obstacles is fixed to 0.2 cm. Two different amounts of obstacles, 5 and 8, are considered here, corresponding to $X = 0.9$ and 1.5 cm of the last obstacle. To reduce computation expenses, a symmetric boundary condition is adopted at the lower boundary, while adiabatic and reflective no-slip boundary conditions are imposed at the other three sides and obstacle surfaces. It is noted that the model without obstacles is the same, except the absence of obstacles. Initially, an artificial hot kernel is set up at the lower left corner to ignite the mixture, surrounded by quiescent homogeneous stoichiometric H_2/air mixture with the initial pressure of $P_0 = 10$ bar. Three initial temperatures,

$T_0 = 915$ K, 935 K and 1000 K, are considered. The initial distributions for temperature and mass fractions of all species inside the hot kernel are extracted from the results computed by the Premix Laminar Flame-Speed Calculation model in Chemkin-PRO [33] for stoichiometric H_2/air at T_0 and P_0. A flame front induced by the hot kernel will propagate from the left to right, and autoignition may take place in the end-gas region between the flame front and right wall in conjunction with the pressure and temperature increase. A detailed reaction mechanism of Li et al. [34] for H_2/air mixture is utilized in the present work. All typical cases discussed below are summarized in Table 1. Note that the dimensions considered here are often applied in the studies of flame propagation in a microscale or narrow channel [35-37] where heat losses to the wall can have a non-negligible impact. However, the heat losses may quantitatively but cannot qualitatively affect the present studies on autoignition transition modes and the elimination of their influence is also more beneficial to focusing on the role of pressure waves in autoignition formation and development.
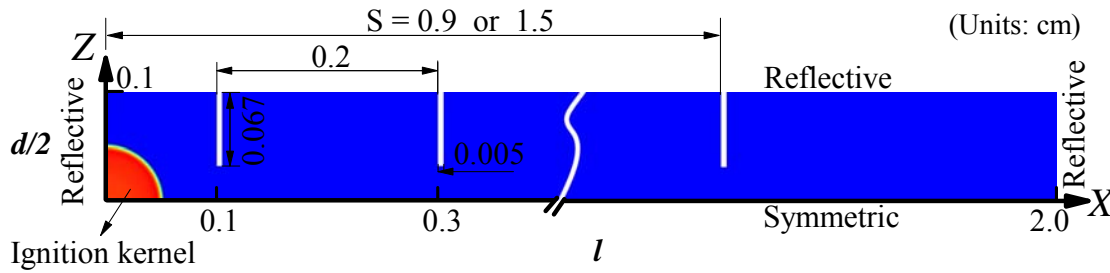
Fig. 1 Computational model. The model without obstacles is the same with this, except the absence of obstacles. S denotes the length covered with obstacles.

Table 1 Typical cases discussed in present work. S =0 means no obstacles

Case	Initial Temperature T_0 (K)	S (cm)	End-gas mode	Peak pressure (atm)	Mean speed of autoignition front (m/s)
1	915	0	No autoignition	30	--
2	915	0.9	No autoignition	44	--
3	915	1.5	Autoignition	245	110 (deflagration)
4	935	0	Autoignition	68	--
5	935	0.9	No autoignition	40	--
6	935	1.5	Autoignition	250	1925 (detonation)
7	1000	0	Autoignition	180	2080 (detonation)
8	1000	0.9	Autoignition	180	2020 (detonation)
9	1000	1.5	Autoignition	210	1900 (detonation)

2.2 Numerical methods

The reactive compressible Navier–Stokes (NS) equations are solved in the present simulations by the parallel adaptive mesh refinement framework Adaptive Mesh Refinement in Object-oriented C++ (AMROC) [38-40]. The time-operator splitting approach, Godunov splitting, is utilized to decouple hydrodynamic transport and chemical reaction source term numerically. The fifth-order accurate Weighted Essentially Non-Oscillatory (WENO) scheme is applied for discretization of the convective part of the NS equations, while the sixth-order accurate Central Difference (CD) scheme is used for the diffusion terms and the third-order Runge-Kutta scheme is used for the temporal integration. The reactive source term is solved by VODE solver [41] within each cell. The thermodynamics properties, transport parameters and reaction rate are evaluated by the Chemkin-II library [42] linked to AMROC. With adaptive mesh refinement method, AMROC can accurately resolve the flame front, shock wave and detonation, and thus has been successfully applied to extensive studies of flame propagation, detonation [38, 43-47],as well as our previous investigation of autoignition [26]. More detailed information on the governing equations and numerical methods can be found in the previous article [26] and thus is not repeated here.

Grid convergence tests are conducted with three different minimum mesh sizes, including 6.25 μm, 3.125 μm and 1.5625 μm while the base cell size keeps 25 μm, corresponding to three, four and five level refinements with the refinement factor of 2. Figure 2 shows the temporal evolutions of the flame tip position and pressure at $(X = 2.0 \text{ cm}, \ Z = 0 \text{ cm})$ at $T_0 = 1000 \text{ K}, \ \text{S} = 0$ and 1.5 cm for these three mesh sizes, respectively. The results indicate that all the grid resolutions can give reasonable evolutions of the flame and pressure waves, while the finest mesh size of 3.125 μm and 1.5625 μm can obtain a better converged solution, so the mesh size of 3.125 μm, corresponding to more than 10 cells per flame thickness and 7 cells per induction length under current initial conditions, is adopted in the present work considering the computational expenses. The same grid configuration is also used in our previous studies of autoignition and detonation development [26] and more validations of grid resolution can be found there.
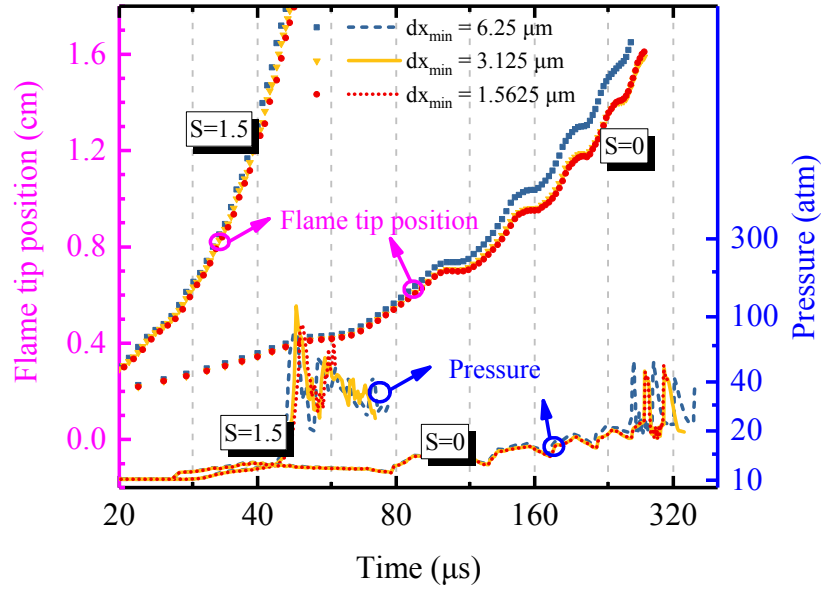
Fig. 2 Temporal evolutions of the flame tip position and pressure at (*X*=2, *Z*=0) with minimum mesh sizes (dx$_{min}$) of 6.25 μm, 3.125 μm and 1.5625 μm, respectively.

3. Results

### 3.1 Flame dynamics and pressure wave evolutions with and without obstacles

End-gas autoignition is attributed to the mixture reactivity increase induced by the pressure wave compression, and the flame propagation can have a great influence on the pressure wave generation whether there are obstacles or not. There have been extensive studies on the flame propagation and flame-pressure wave interactions in smooth and obstructed channels [24, 48-50], which have deeply improved our understanding of the underlying mechanisms. Thus, in this section, we briefly discuss the evolutions of flame and pressure waves in a closed chamber, taking case 7 ($T_0 = 1000$ K, S = 0) and case 9 ($T_0 = 1000$ K, S = 1.5) as examples, which is not aimed at further investigating above mechanisms but at highlighting the process difference in such confined space and at contributing to a better understanding of the pressure wave-induced autoignition process as discussed below. Figure 3(a) shows the flame and pressure wave configurations without obstacles (case 7). As can be seen, after ignited by the hot kernel, a semispherical flame develops and gradually involves into the finger shape due to the constrains of upper and bottom walls, which increases the flame surface area and thus results in faster energy release. A pressure wave is clearly observed ahead of the flame front because of the rapid expansion of the latter at 6 μs. Because of the large speed difference between the

flame and the pressure wave, the latter propagates back and forth in the closed chamber after reflections at the right and left walls, and interactions with the flame time after time, which results in the flame instability, and wrinkles are observed along the flame front. Actually, pressure waves are generated continually as the flame propagates, some of which can catch up with this strongest pressure wave and coalesce with it, but some not. Note that this strongest pressure wave dominates the reactivity increase of the end-gas [26]. As shown at 279 μs, a detonation wave is observed, induced by the end-gas autoignition. It should be noted that the end-gas is also possibly consumed by the flame and no autoignition occurs as discussed below. Figure 3(b) shows the flame and pressure wave configurations with obstacles (case 9). Extremely different from case 7, an intensively turbulent flame is developed in this case because of the disturbance of the obstacles. The studies by G. Ciccarelli et al. [50] indicate that driven by the expansion of flame front, the unburned mixture ahead of the flame front moves downstream, and multiple scales of turbulence are generated in the flow field, thus resulting in a highly wrinkled flame surface in turn. The propagation of the turbulent flame is obviously faster than that in case 7, and it takes only about 45 μs for the flame to pass the last obstacle at $X = 1.5$ cm. After that, two strong pressure waves are observed ahead of the flame front, whose reflections at the right wall immediately induce end-gas autoignition as shown at 48.5 μs. Note that the overall process of the flame propagation and pressure wave development in other cases is similar to that in these two cases and not discussed here.


(a)

(b)
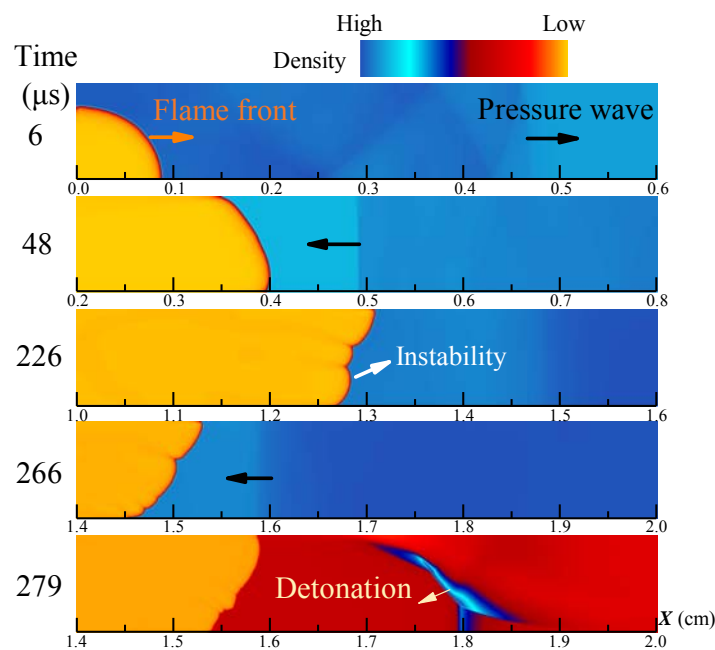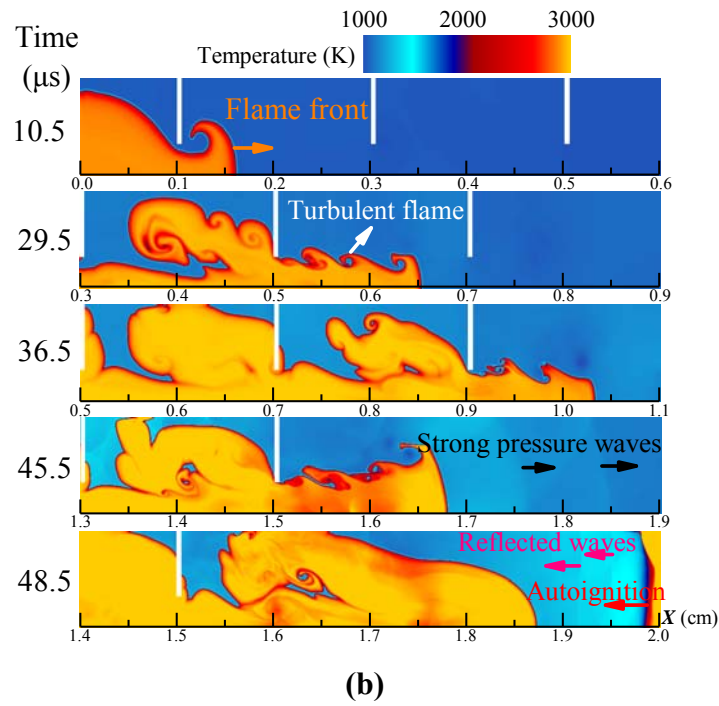
Fig. 3 Sequences of flame and pressure wave configurations at $T_0 = 1000$ K, S = 0 (a) and 1.5 cm (b)

The evolutions of the flame tip position and the flame speed as functions of time and the flame tip position respectively in all nine cases are shown in Fig. 4. Note that the flame tip is defined as the right most tip along the flame front. The flame tip position is defined as the distance from the flame tip location to the left side wall and the flame speed is calculated based on the temporal derivative of the flame tip position. As can be seen in Fig. 4 (a), initial temperature has a more evident effect on the flame speed in the cases without obstacles, while the flame acceleration induced by obstacles dominates the flame speed in the cases with obstacles and only a slight difference can be observed under different initial temperatures when the number of obstacles is the same. Fig. 4 (b) shows that although the flame speeds in the cases without obstacles show oscillations as a result of the flame-pressure wave interactions, the mean speeds keep nearly constant. More violent oscillations of flame speeds are observed in the cases with obstacles, but the mean speeds in these cases have a powerful increase after the flame passes every obstacle, which is consistent with these previous studies on flame acceleration in obstructed channels [49-51]. The mean flame speeds reach up to about 800 m/s in the cases with S = 1.5 cm. In addition, more attention should be drawn to the flame speed evolutions with S = 0.9 cm, which comprises three distinct stages in terms of the flame tip position. The first stage is before $X = 1$ cm, during which the flame speeds with S = 0.9 cm keep the same growing trend as that with S = 1.5 cm thanks to the same obstacle configuration. The mean speeds reach up to

about 600 m/s in this stage. When the flame front has passed the last obstacle, the speeds decrease to about 450 m/s and keep this value before $X = 1.65$ cm, which we denote the second stage. In the third stage, it is noted that the flame speeds have an abrupt decrease at $X = 1.65$ cm. This is because the flame front interacts with the strong pressure wave propagating to the left. After that, the flame accelerates once again as a result of its development into a fingering flame, which increases the flame surface area and thus promote the heat release. The flame evolutions in the third stage will be clearly seen in the following sections.
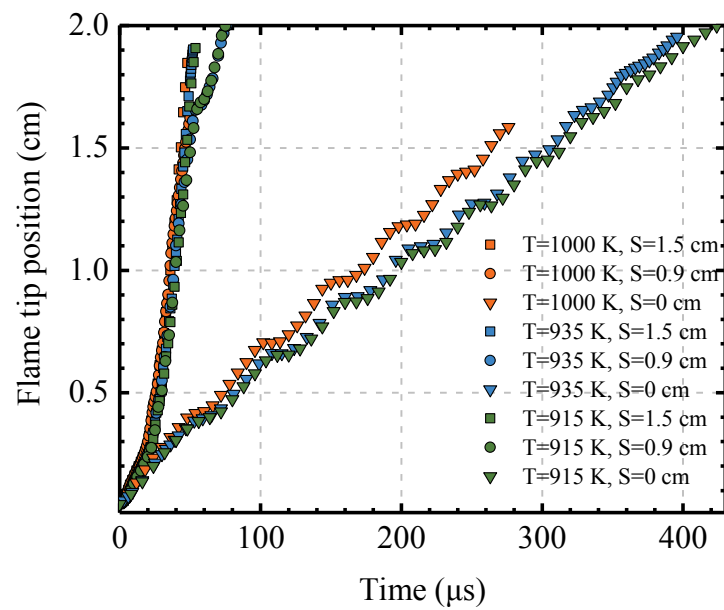

(a)
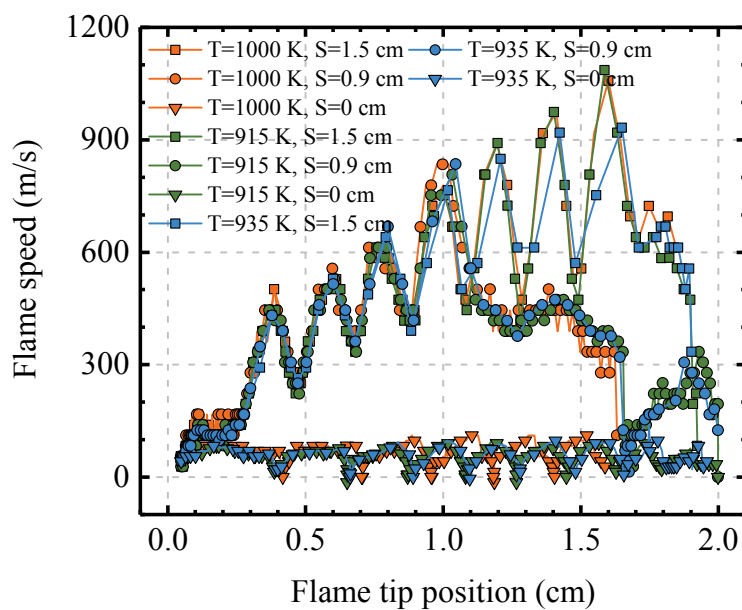
(b)

Fig. 4 Evolutions of flame tip position (a) and flame speed (b) as functions of time and the flame tip position respectively in all cases

3.2 Autoignition promoted by a long column at $T_0 = 915$ K

Figure 5 shows the flame and pressure wave evolutions when the flame approaches the end wall in the cases at $T_0 = 915$ K. It should be noted that Fig. 5(a) is for case 2 while Fig. 5(b) and (c) are both for case 3. Case 1 is not shown here considering that the overall process of flame propagation is similar to that in case 7 as discussed in Section 3.1 except no autoignition occurrence before the flame reaches the end wall. In addition, the flame evolutions in the early stage in these cases are also similar to that mentioned above and not discussed here. As shown in Fig. 5(a), it is observed that multiple reflected pressure waves propagate in the end-gas. Specifically, RPW1 and RPW2 are pressure waves generated by the flame acceleration and reflected at the right end wall. RPW3 is the reflected pressure wave of the interaction of RPW1 with the flame front and RPW4 is generated by the reflection of RPW1 on the last obstacle at $X = 0.9$ cm. At 55 μs (A2), the flame interacts with RPW1 at about $X = 1.65$ cm, which is exactly corresponding to the position where the flame speeds abruptly decease in Fig. 4(b), as explained above. Then the flame front interacts with RPW4 propagating to the right. These interactions result in the formation of a finger flame, whose surface area continually increases until it reaches the end wall, leading to the flame acceleration in the third stage, as discussed above. Afterwards, the flame consumes the whole fresh mixture and autoignition does not occur in this case. However, with addition of obstacles to $X = 1.5$ cm in case 3, autoignition occurs firstly at the upper right corner (AIF1) and then at the center (AIF2) as shown in Fig. 5(b). It is noted that the autoignition only leads to the deflagration propagation in the early stage until a detonation wave develops induced by the interactions between the complicated pressure wave configurations and the autoignition front close to the upper wall. A closer observation (not shown here) indicates that the location of detonation initiation coincides with the contact point between two pressure waves propagating at opposite directions, where an extremely high pressure is obtained and induces the detonation. Actually, this detonation initiation process is also similar to the observations in other studies [14, 20, 21], where the strong pressure waves generated by the first autoignition kernel lead to the detonation development of the second autoignition kernel. The detonation wave rapidly consumes the rest of fresh mixture within 1 μs and then degenerates to a shock wave. In addition, it is shown that a much shorter finger flame is developed because of the reduced distance between the last obstacle and the right end wall in case 3, so the second acceleration is not clearly observed in Fig. 4(b).
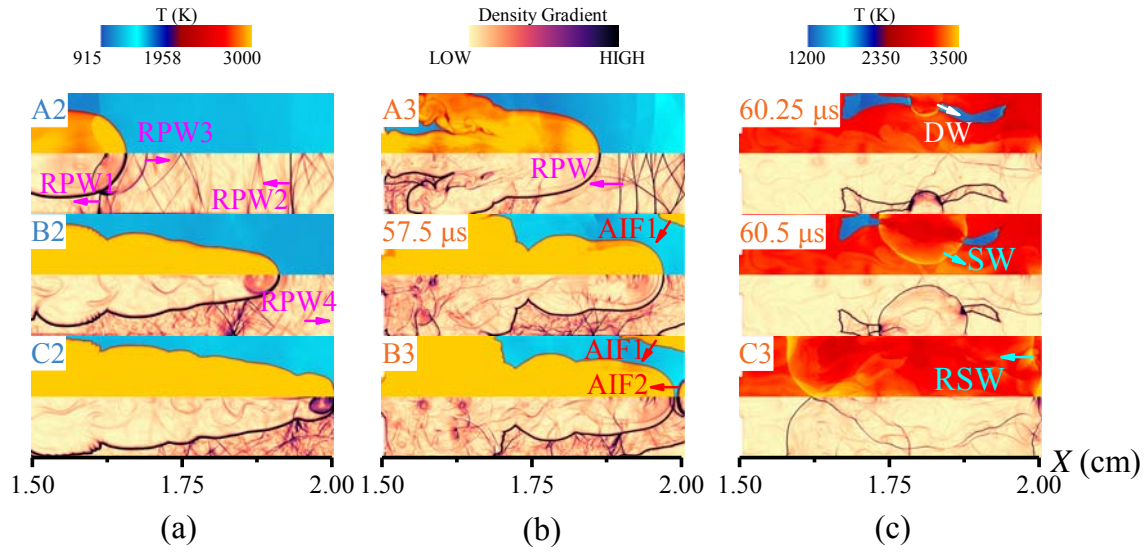
Fig. 5 Sequence of images composed of temperature contour (upper) and density gradient (lower) when the flame approaches the end wall at $T_0 = 915$ K. (a) case 2, (b) and (c) case3. RPW-Reflected pressure wave; AIF-Autoignition front; DW-Detonation wave; SW-Shock wave; RSW-Reflected shock wave. Physical times of snapshots not listed above: A2-55 μs, B2-71 μs, C2-75 μs, A3-52.75 μs, B3-58.5 μs, C3-61.25 μs.

To further investigate the effects of pressure wave on the end-gas autoignition, Figure 6 shows the temporal evolutions of pressure (a), OH mass fraction and temperature (b) at $(X = 2.0$ cm, $Z = 0$ cm) in the cases at $T_0 = 915$ K. The OH mass fraction is selected here to identify the reactivity of the unburned mixture and the instant when OH mass fraction reaches up to 10^{-5} is regard as the onset of autoignition. It is shown that there is only weak pressure oscillation in case 1 without obstacles as the pressure wave propagates back and forth in the chamber. The mean temperature and OH mass fraction are gradually increased with the pressure wave reflections, and reach up to 1200 K and 10^{-7}, respectively, before the flame arrives at the end wall. No autoignition occurs and the maximum pressure reaches up to the equilibrium pressure of about 30 atm in case 1. Although autoignition does not take place in case 2 either, instead a larger pressure oscillation is observed from 50 to 90 μs, thanks to the reflections of strong pressure waves generated by flame acceleration. After compressions by RPW1 and RPW2 as shown at 55 μs (A2), the temperature and OH mass fraction of the local mixture is increased to 1300 K and decreased to 10^{-9}, respectively in case 2. However, this more favorable conditions for autoignition cannot be maintained after the pressure waves leave the end wall. After that, the temperature decreases to only 1100 K, and no more OH is largely produced,

such that autoignition does not occur before the flame arrives at the end wall. Nevertheless, an entirely different situation happens in case 3 with addition of obstacles to $X = 1.5$ cm. More powerful pressure waves are generated by the stronger flame acceleration in this case, which compress the local mixture to 60 atm, 20 atm larger than that in case 2, and bring about the higher post-compression temperature of 1400 K and OH mass fraction of 10^{-8}, respectively, as shown in Fig. 6(b). It is especially noted that although the temperature decreases like that in case 2 after pressure waves leave, the OH mass fraction keeps steadily increasing, which promotes the reactivity of mixture and consequently results in the autoignition occurrence in case 3. To further identify the effects of end-gas combustion mode on pressure oscillation, Fig. 7 shows pressure evolutions as a function of specific volume for $(X = 2, Z = 0)$ in these three cases. It is indicated that the location of the pressure transducer experiences a constant pressure combustion mode in all three cases. However, the combustion mode is dominated by flame propagation in case 1 and case 2, while it is induced by autoignition that leads to deflagration in case 3. It is also showed that the maximum pressure of the track point reaches up to 175 atm after compression by the shock wave degenerated from the detonation wave in case 3, which is much larger than that in case 1 and case 2 without autoignition.

(a)

(b)
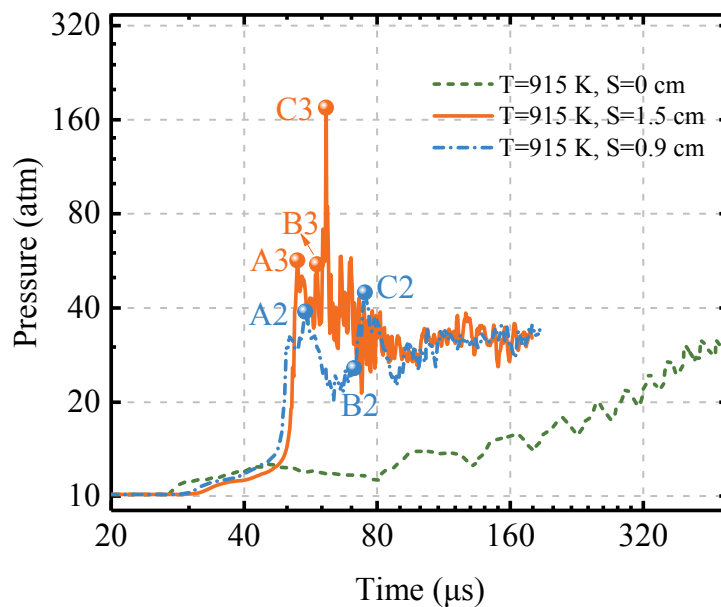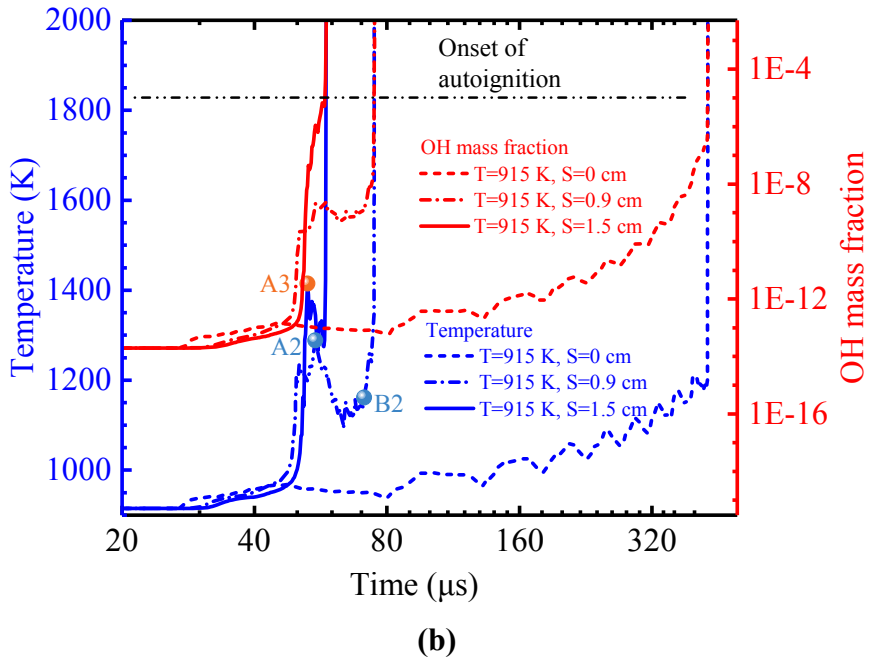
Fig. 6 Temporal evolutions of pressure (a), temperature and OH mass fraction (b) for $(X = 2, Z = 0)$ in the cases with $T_0 = 915$ K. The representative points denoted as A2, B2 and A3 correspond to those in Fig. 5.
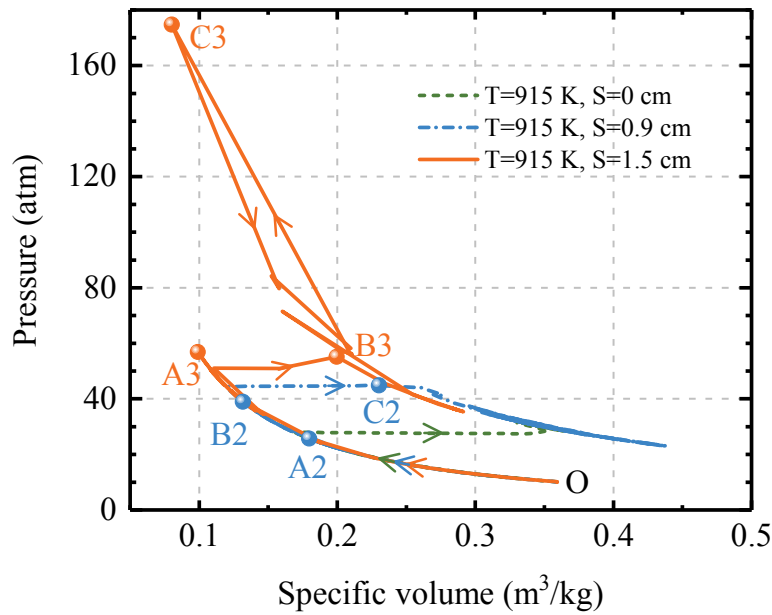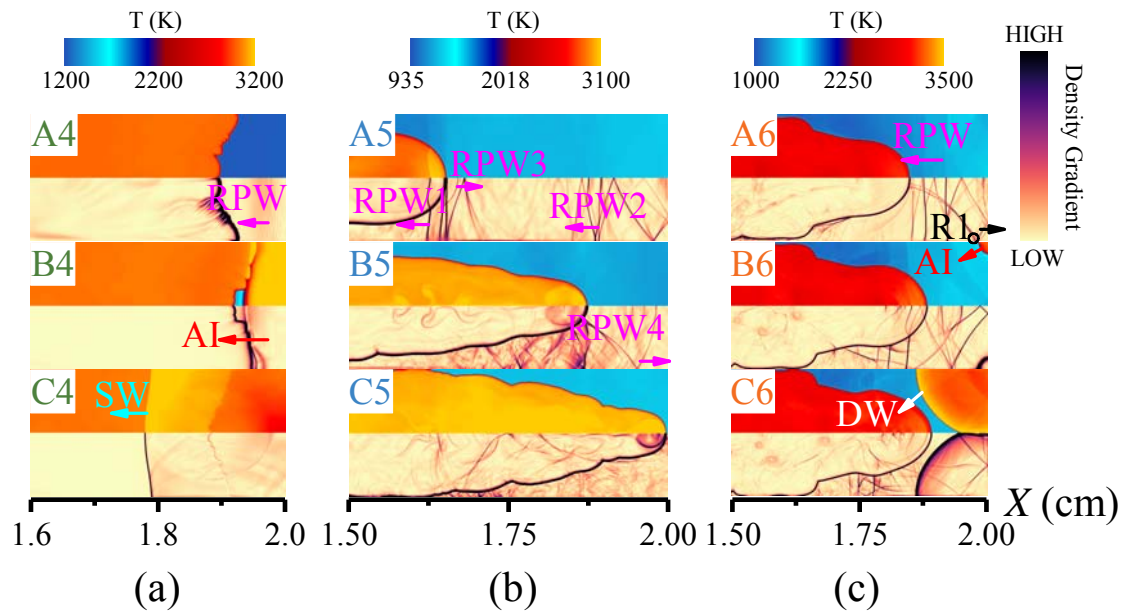

Fig. 7 Pressure evolutions as a function of specific volume for $(X = 2, Z = 0)$ in the cases with $T_0 = 915$ K. The representative points denoted as A2 to C3 correspond to those in Fig. 5.

3.3 Autoignition delayed by a short obstacle column at $T_0 = 935$ K

Different from no autoignition to autoignition transition in the cases at $T_0 = 915$ K, the transition takes place twice, including autoignition to no autoignition and no autoignition to

autoignition again, as the initial temperature increases to 935 K. Fig. 8 shows the flame and pressure wave evolutions for case 4 (a), case 5 (b) and case 6 (c), while Fig. 9 shows the temporal evolutions of pressure (a), temperature and OH mass fraction (b) in these cases. As clearly shown in Fig. 8(a), the autoignition takes place at almost the same time in the whole end-gas region at 397.8 µs (B4), which is identified as thermal explosion in Bradley's diagram as discussed later. The pressure evolution before autoignition is similar to that in case 1 and only a slight oscillation can be observed, while the autoignition generates the stronger pressure oscillation with the maximum pressure of 60 atm in case 4. The temperature before autoignition reaches 1240 K, a little higher than that in case 1, while the OH mass fraction reaches up to 10^{-6}, an order of magnitude higher than that in case 1. This shows the slightly elevated initial temperature promotes larger accumulation of OH in the end-gas during the flame propagation, which improves the reactivity of the mixture and thus results in the autoignition before the flame reaches the end wall. However, the autoignition is suppressed with addition of obstacles to 0.9 cm in case 5. As shown in Fig. 8(b), the flame and pressure wave profiles in this case are extremely similar to that in case 2 and not discussed repeatedly. Although the post-compression temperature reaches 1300 K, a little higher than that before autoignition in case 4, the OH mass fraction is much lower in case 5, along with the temperature decrease after pressure waves leave, which largely reduces the reactivity of mixture. Thus, the end-gas is consumed by the accelerated flame and autoignition is suppressed. When the obstacles are extended to 1.5 cm, autoignition occurs again in case 6. As shown in Fig. 8(c), the autoignition takes place at the upper right corner after a pressure wave (denoted as R1) reflects at that location. Different from the deflagration induced by autoignition in case 3, the autoignition in case 6 rapidly develops into a spherical detonation wave at 53 µs (C6). Fig. 10 shows the pressure evolutions as a function of specific volume for $(X = 2, Z = 0)$ in the cases with $T_0 = 935 \, \text{K}$. Three distinct end-gas combustion modes, including constant pressure combustion for case 5 without autoignition, nearly constant volume combustion for case 6 with detonation development and combustion between the first two modes for case 4 with thermal explosion, are observed. It is also noted that the maximum pressure in the transducer location is increased with a switch of the combustion mode from constant pressure to constant volume as shown in Fig. 9(a).
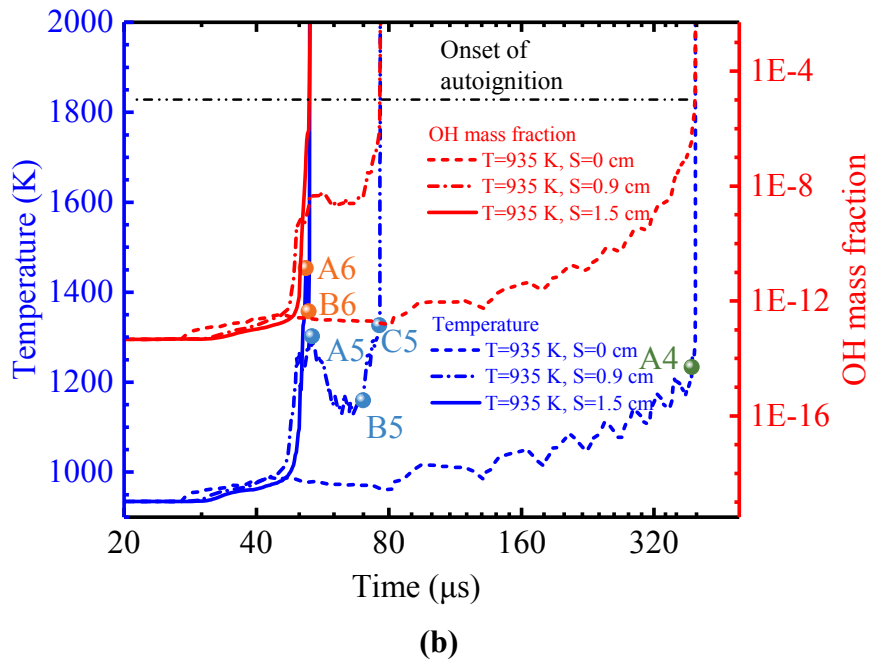
Fig. 8 Sequence of images composed by temperature contour (upper) and density gradient (lower) when the flame approaches the end wall at $T_0 = 935$ K. (a) case 4, (b) case 5 and (c) case 6. AI-Autoignition. Other abbreviations are the same as in Fig. 5. A4-390 µs, B4-397.8 µs, C4-398.8, A5-53.5 µs, B5-70 µs, C5-76 µs, A6-51.75 µs, B6-52.5 µs, C6-53 µs.

(a)

(b)
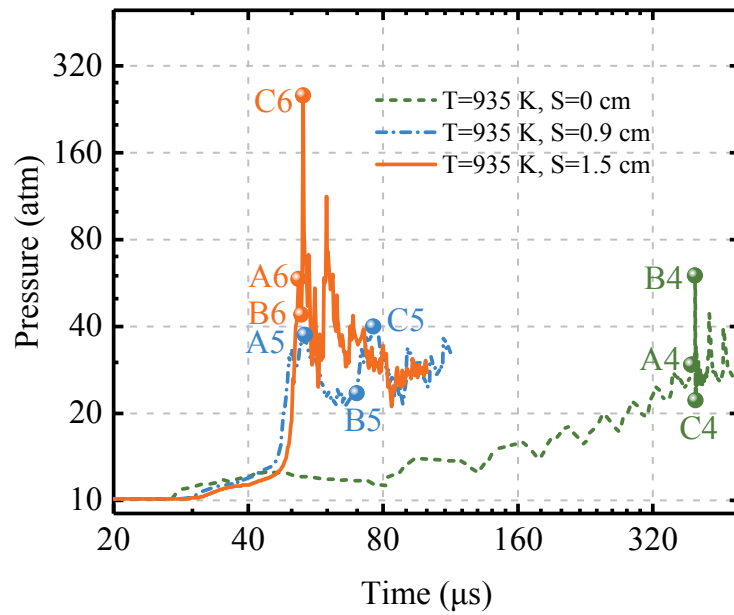
Fig. 9 Temporal evolutions of pressure (a), temperature and OH mass fraction (b) at $(X = 2, Z = 0)$ **in the cases with** $T_0 = 935$ **K. The representative points denoted as A4 to B5 correspond to those in Fig. 8.**
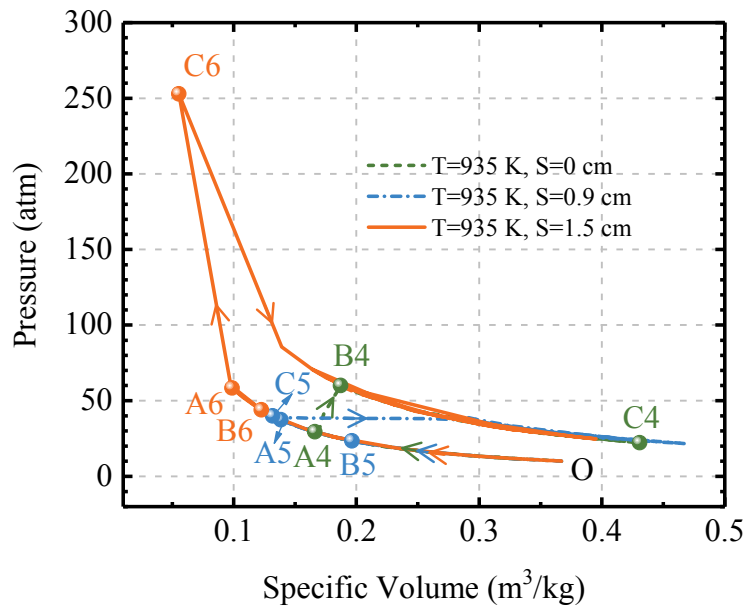

Fig. 10 Pressure evolutions as a function of specific volume for $(X = 2, Z = 0)$ **in the cases with** $T_0 = 935$ **K. The representative points denoted as A4 to C6 correspond to those in Fig. 8.**
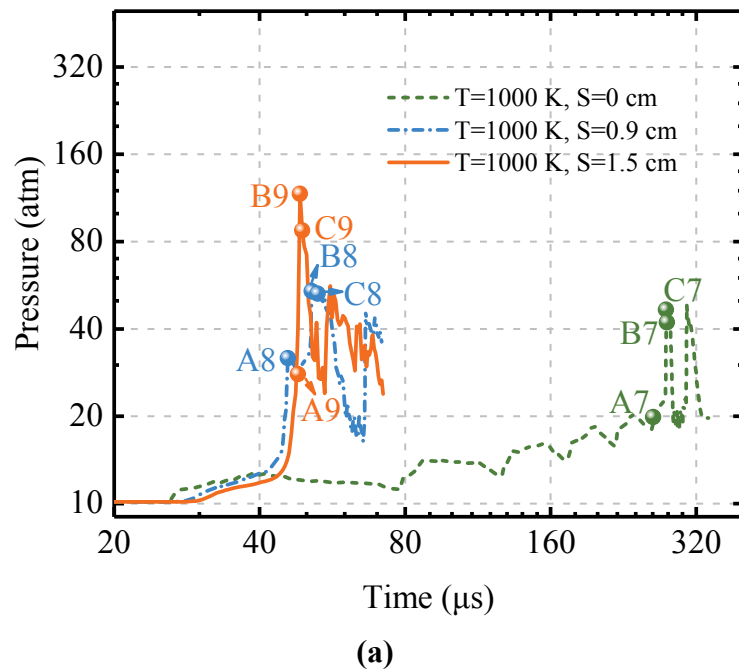
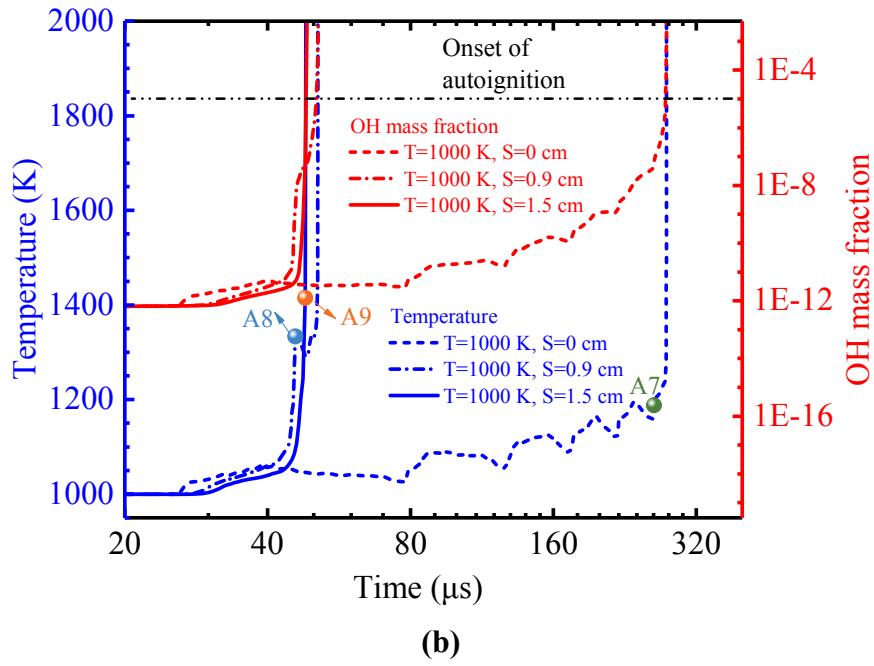### 3.4 Autoignition independent of obstacles at $T_0 = 1000$ K

When the initial temperature increases to 1000 K, autoignition can never be suppressed and

it takes place in all three cases no matter there are obstacles or not, as shown in Fig. 11. In case 7 without obstacles, thermal explosion similar to case 4 takes place in the region near the end wall at 277.25 μs (B7), while the flame just arrives at $X = 1.6\ \text{cm}$ at the time, which leaves more space for the autoignition to propagate such that it consequently develops into a detonation wave at 278.5 μs (C7) as shown in Fig. 11(a). In case 8, the post-compression temperature and OH mass fraction in the transducer location are up to 1330 K and above 10^{-8} respectively, which is slightly higher than in cases 2 and 5. However, it is this slight difference that makes the reactivity of mixture be able to keep increasing after the pressure waves leave and finally results in autoignition. As the obstacles are further extended to 1.5 cm in case 9, autoignition takes place at the instant when the pressure waves are reflected at the right wall and neither of the temperature and OH mass shows a staged evolution before autoignition, compared to other cases with obstacles, as can be seen in Fig. 12(b). In addition, a detonation wave is developed in both case 8 and case 9. It should be noted that the recognition of detonation in the present work is based on the autoignition front propagation speeds and the 1D profiles of the pressure and temperature along the direction of autoignition front propagation. The latter is not shown here due to the limited space, while the former is summarized in Table 1. Note that the mean speeds of these autoignition fronts that develop into detonation waves are basically at 2000 m/s, all close to the local Chapman-Jouguet (CJ) detonation speeds. Furthermore, by comparisons of these cases with and without autoignition at all three initial temperatures, it is shown that there seems to be a critical state represented by the temperature and OH mass fraction, and once the reactivity of the mixture is above this state under the help of external force, such as the pressure wave compression, it is able to accelerate the reaction progress spontaneously until the autoignition occurs, as observed in case 3, case 6 and so on, which may have associations with the chain-branching chemistry reaction and accumulation of radicals. Moreover, dramatic pressure oscillations are observed and the end-gas combustion mode prefers to constant volume in all three cases as shown in Fig. 12(a) and Fig. 13, respectively.
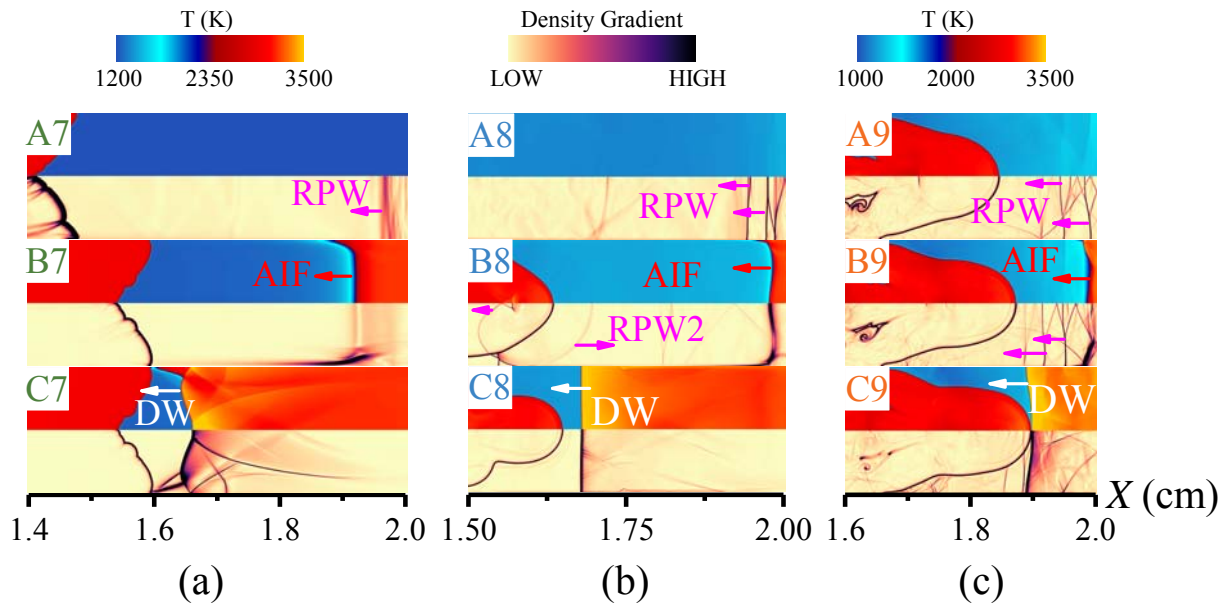
Fig. 11 Sequence of images composed by temperature contour (upper) and density gradient (lower) when the flame approaches the end wall at $T_0 = 1000$ K. (a) case 7, (b) case 8 and (c) case 9. PW-Pressure wave. Other abbreviations are the same as in Fig. 5. A7-261 μs, B7-277.25 μs, C7-278.5 μs, A8-45.75 μs, B8-51.25 μs, C8-52.75 μs, A9-48 μs, B9-48.5 μs, C9-49 μs

(a)

(b)

Fig. 12 Temporal evolutions of pressure (a), temperature and OH mass fraction (b) at

$(X = 2, Z = 0)$ **in cases with** $T_0 = 1000$ **K. The representative points denoted as A7, A8 and**

A9 correspond to those in Fig. 11.
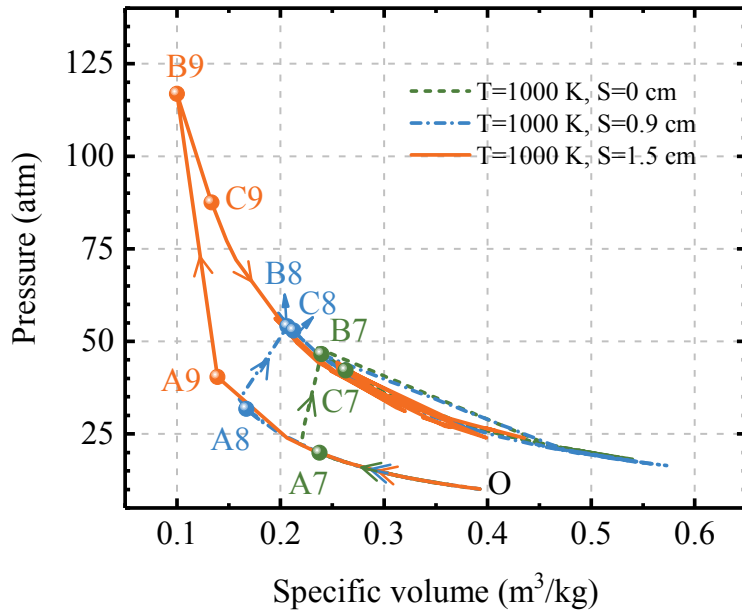
Fig. 13 Pressure evolutions as a function of specific volume for $(X = 2, Z = 0)$ **in cases with**

$T_0 = 1000$ **K. The representative points denoted as A7 to C9 correspond to those in Fig. 11.**

4. Discussions

4.1 Different autoignition transition modes

The nine cases in Section 3 give three different autoignition transition modes: no autoignition to

autoignition, autoignition to no autoignition to autoignition again and autoignition invariably. According to above results, it can be that the initial temperature and pressure waves play a vital role in these transition modes. Some previous studies have observed autoignition to no autoignition transition with elevated flame speed [31, 32]. However, multiple transition modes and especially transitions twice like in cases at $T_0 = 935 \text{ K}$ may be proposed in the present studies for the first time. In addition, there are seldom studies, whose analyses are based on pressure waves, for competition between flame propagation and end-gas autoignition. Considering the simulations is discrete, a question is that whether there are only these three transition modes with the continuous variation of the initial temperature and pressure wave intensity. Nevertheless, investigating the trend of autoignition transition by conducting plenty of numerical simulations is impractical considering the complicated physical phenomenon and huge computational cost. Therefore, an idealized model is presented here as shown in Fig. 14, where the flame ignited by the hot kernel propagates from the left end wall to right end wall, which generates a pressure wave ahead of the flame front. This model is actually similar to that in these cases without obstacles. The autoignition transition is intrinsically the comparison between the ignition delay time of the end-gas and the duration of flame propagation from left end wall to right end wall. When the ignition delay time is less than the flame propagation duration, autoignition occurs, and on the contrary, it does not occur. Thus, for the convenience of evaluating these two key parameters, two assumptions are adopted here. One is that the flame propagates at a constant speed, so that the flame propagation duration can be obtained easily from dividing the chamber length by this speed. The other is that the pressure wave reflects on the right end wall only once before the flame reaches the right end wall. This assumption can make it easy to evaluate the effects of pressure wave reflection on the ignition delay time of the end-gas mixture. The effects of difference between these two assumptions and the reality will be discussed later. Then it is necessary to link the flame propagation with the autoignition. And there is nothing more appropriate than pressure wave to be the intermediary between them. In previous studies, Bradley et al. [52] proposed formulas that relate the flame speed with the Mach number of the shock ahead of the flame to investigate DDT in a duct, which is also appropriate for the flame propagation process here. Some formulas relevant to the present work are repeated as below:

According to mass conservation, the flame speed can be given by

$$S_f = \left(\frac{A}{a}\right)\sigma u_t, \qquad \text{with } \sigma = \frac{\rho_u}{\rho_b} \tag{1}$$

Here S_f is the flame speed. A is the flame surface area. a is the cross-sectional area of the duct. ρ_u is the unburned gas density. ρ_b is the burned gas density. u_t is the turbulent burning velocity.

The expansion of the burned gas creates a gas velocity, S_g, along the duct ahead of the flame in the direction towards the shock which is given by

$$S_g = \frac{A u_t}{a}(\sigma - 1) \tag{2}$$

From Eqs. (1) and Eqs. (2), it can be given

$$S_g = S_f \frac{(\sigma - 1)}{\sigma} \tag{3}$$

On the other hand, the gas velocity, S_g, can be also given by the shock wave equations as

$$S_g = \frac{2(Ma^2 - 1)a_1}{(\gamma + 1)Ma} \tag{4}$$

Here, Ma is the Mach number of the shock, relative to the unburned gas. a_1 is the sound speed in the unburned mixture. γ is the specific heat ratio.

From Eqs. (3) and Eqs. (4), it can be given

$$S_f = \frac{\sigma}{\sigma - 1} \cdot \frac{2(Ma^2 - 1)a_1}{(\gamma + 1)Ma} \tag{5}$$

It should be noted that Eqs. (3) and Eqs. (5) are derived in the present work based on other equations. Eqs. (5) gives the relationship of the flame speed with the Mach number of the shock wave generated by the flame. Then it is needed to find the relationship of ignition delay time with the Mach number. Based on the second assumption, the ignition delay time of the mixture can be obtained with the thermodynamic parameters after the pressure wave reflection as the initial conditions. According to Ref.[53], the temperature and pressure of the end-gas after pressure wave reflection can be evaluated by
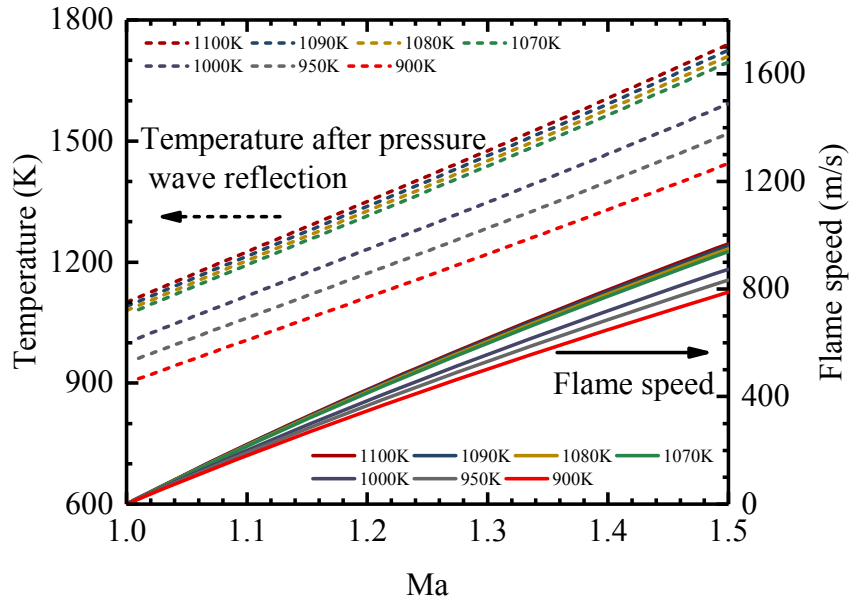
$$T_a = \frac{[2(\gamma - 1)Ma^2 - (\gamma - 3)][(3\gamma - 1)Ma^2 - 2(\gamma - 1)]}{(\gamma + 1)^2 Ma^2} T_b \tag{6}$$

$$P_a = \frac{[2\gamma Ma^2 - (\gamma - 1)][(3\gamma - 1)Ma^2 - 2(\gamma - 1)]}{(\gamma + 1)[(\gamma - 1)Ma^2 + 2]} P_b \tag{7}$$

Here, the subscript b and a denote the mixture state before and after pressure wave reflection.
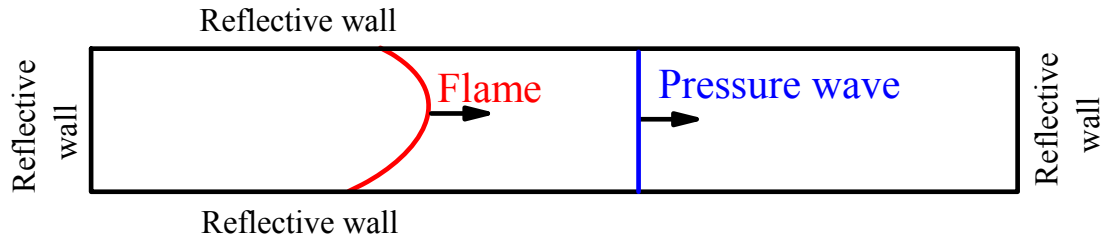
Fig. 14 Schematic of the idealized physical model

Fig. 15 Evolutions of temperature after pressure wave reflection and flame speed as functions of Mach number under different initial temperatures according to Eqs. 5 and 6, respectively.

Fig. 15 shows the evolutions of the temperature after pressure wave reflection and the flame speed as functions of Mach number under different initial temperatures obtained from Eqs. 5 and Eqs. 6 respectively. The parameters in the equations, such as the sound speed a_1, the specific heat ratio γ, are calculated based on the stoichiometric H_2/air mixture at corresponding temperatures. The results show that the flame speed and the temperature after pressure wave reflection both expectedly increase with the elevated Mach number and initial temperature. In addition, it should be noted that Fig. 15 gives a reasonable prediction for the relationship of flame speed and temperature after pressure wave reflection in above simulations, which is beneficial to the comparison between the flame propagation duration and the ignition delay time. For example, in case 5 ($T_0 = 935$ K, $S = 0.9$ cm), the flame speed stays at about 450 m/s, and the temperature of the unburned mixture approaches 1000 K before the pressure wave reflections as shown in Fig. 4(b) and Fig. 9(b) respectively, which can give the Mach number of about 1.24 from Fig. 15, and further it can be obtained that the corresponding temperature after pressure wave reflection is about 1300 K, consistent with the

simulation. In case 6 with $S = 1.5$ cm, the flame speed is about 700 m/s and the temperature also approaches 1000 K before the pressure wave reflections, which can give a Mach number of about 1.39, and further come up with the temperature of 1450 K, consistent with the simulation as well.

After getting the flame speed and thermodynamics parameters (temperature and pressure) of the end-gas after pressure wave reflection, the flame propagation duration can be evaluated from dividing the chamber length by the flame speed, and the ignition delay time can be obtained from Chemkin PRO with the mixture state after pressure wave reflection as initial conditions. Fig. 16 shows the profiles of ignition delay time and flame propagation duration as functions of Mach number under different initial temperatures. Here, the chamber length is 2 cm and the fresh gas is the stoichiometric H_2/air mixture. It is noted that different amounts of intersection points between the ignition delay time and flame propagation duration are observed with increase of the initial temperature, which exactly represents the different autoignition transition modes. At the lower initial temperature, such as 900 K, 950 K in Fig. 16, there exist two intersection points theoretically. However, the left point is extremely close to $Ma = 1$ and the corresponding flame propagation duration is infinite, which means there is no flame propagation in the chamber. Thus, this intersection is meaningless for the present studies. Hence, there is only one intersection located at larger Mach number under each lower initial temperature. The left part of the intersection means no autoignition because the ignition delay time is larger than the flame propagation duration and on the contrary, the right part means autoignition, which agrees with the no autoignition to autoignition transition mode in the simulations at $T_0 = 915$ K. With increase of the initial temperature to about 1070 K, the left intersection located at lower Mach number becomes meaningful, which corresponds to a lower flame speed, like flame propagation in a chamber without obstacles. Thus, there are two intersection points under this initial temperature range as clearly shown in enlarged view in Fig. 16, which represent autoignition to no autoignition transition and no autoignition to autoignition transition, respectively. This mode agrees with the simulations at $T_0 = 935$ K. It is also shown that when autoignition occurs at lower Mach number, the ignition delay time is greatly close to the flame propagation duration, which is very similar to the scenario in case 4, where the flame front approaches the right end wall before the autoignition occurrence. Further increasing the initial temperature to 1100K and over, the ignition delay time is always lower than the flame propagation duration and no intersection is observed, which means autoignition takes place all the time. This mode agrees with the simulations at $T_0 = 1000$ K.

It is noted that the initial temperatures in Fig. 16 are all higher than that in the simulations with the same autoignition transition modes. This is to a great extent caused by the second assumption. In fact, the pressure wave should reflect on the wall more than one time before the flame reaches the end wall. The smaller the Mach number is, the more times the pressure wave reflects, and further the more the ignition delay time decreases, while at larger Mach number, the ignition delay time is nearly equal to that in Fig. 16, which will make the ignition delay time curves bend anticlockwise. Therefore, the corresponding autoignition transition modes will shift to the lower initial temperature. As to the first assumption, it does not have an influence on the cases without obstacles, where the mean flame speed is basically constant as discussed above, while for the cases with obstacles, the flame propagation duration should be a little longer. However, this difference can only make the intersection at larger Mach number have a slight shift and not have an obvious influence on the autoignition transition modes.

Based on Fig. 16, a diagram of different autoignition transition modes, with the initial temperature and Mach number as limits, can be qualitatively proposed, as shown in Fig. 17. Three different transition modes, including one transition at the lower initial temperature, two transitions at the moderate temperature and zero transition at the higher initial temperature, are divided by the upper and lower limits of initial temperature, designated by T_u and T_l, respectively. It should be noted that the initial temperature here inherently represents the reactivity of mixture and thus can be also extended to equivalence ratio and so on. In the one-transition zone, a limit of Mach number, denoted as Ma_0, which is composed of the right intersection points at larger Mach number in Fig. 16, divides the zone into two parts. The left part is no autoignition while the right part is autoignition. This limit decreases with the increase of the initial temperature. It means that the higher the initial temperature is, the weaker the pressure wave that is needed to induce the transition from no autoignition to autoignition. At the two-transition zone, two limits of Mach number, Ma_1 and Ma_2, surround a no-autoignition zone, and this zone gradually reduces with the initial temperature and finally disappears, and hence the zero-transition zone is formed at the high initial temperature. In fact, the Mach number here can represent the intensity of pressure waves in real engine conditions. The pressure waves generated by the normal flame propagation are usually weaker, which means lower Mach number here, while under pre-ignition and multiple hot-spot autoignition conditions, the pressure waves generated by autoignition are usually stronger and can induce other hot-spot autoignition directly [14,

20, 54], corresponding to the larger Mach number here. In fact, Fig. 17 also involves the autoignition to no autoignition transition mode in previous studies [31, 32], where the pressure waves in these studies are generated by the normal flame propagation and should be weaker with lower Mach number. Therefore, this transition is exactly corresponding to the zones on both sides of the limit Ma_1. Moreover, Fig. 17 also shows that if the mixture is highly reactive (like at the high temperature), or the pressure wave is stronger enough, the autoignition cannot be suppressed intrinsically.
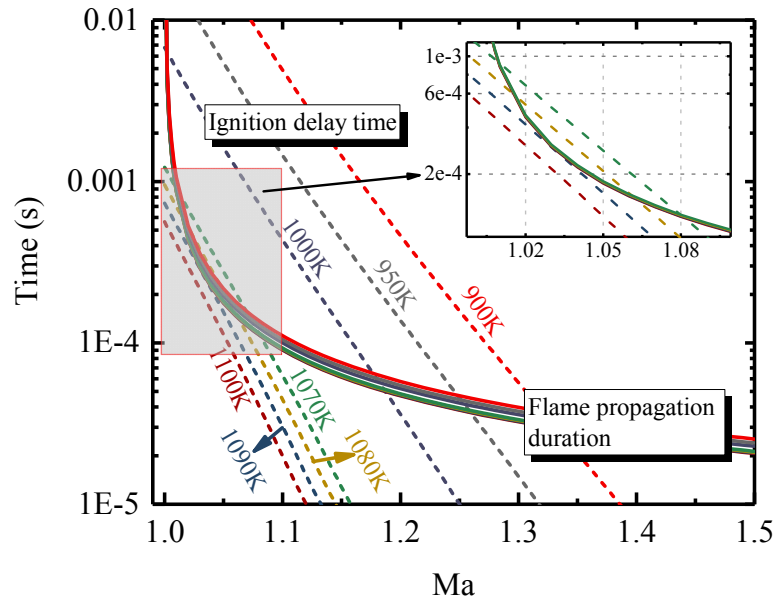
Fig. 16 Profiles of ignition delay time and flame propagation duration in a closed chamber as functions of Mach number under different initial temperatures.
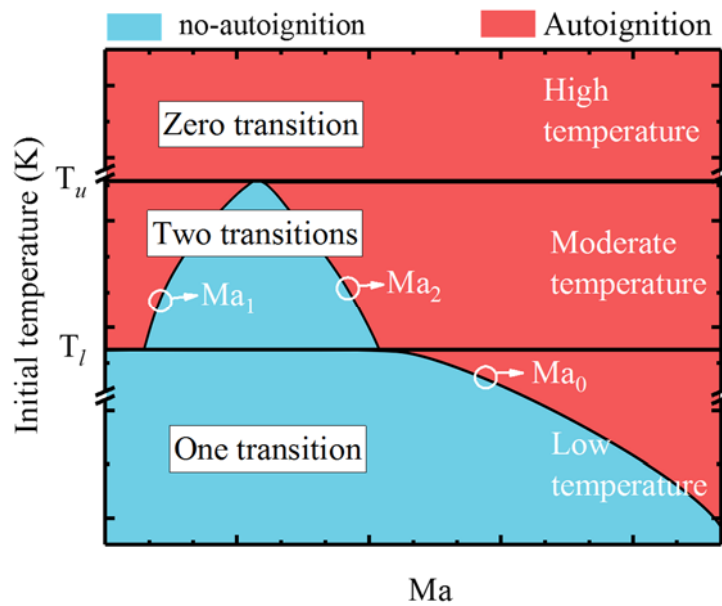
Fig. 17 Diagram of different autoignition transition modes

4.2 Different autoignition propagation modes

Section 4.1 discusses the different autoignition transition modes, which mainly aims to investigate whether autoignition can take place. However, in the scenarios with autoignition, different propagation modes of hot spots can be developed, which directly has an influence on the intensity of pressure oscillation in the chamber after autoignition. Therefore, this section further discusses the effects of pressure wave on autoignition propagation modes. Bradley's diagram [6-8] is introduced here to analyze the development of end-gas autoignition in the above simulations. There are two non-dimensional parameters, ξ and ε, in Bradley's diagram, where ξ represents the coupling between acoustic wave and reaction front and ε is a measure of the energy transfer into the developing acoustic front at a hot spot. They are given by the following formulas:

$$\xi = \frac{a}{u_a} = \frac{a}{\left(\frac{\partial \tau_i}{\partial r}\right)^{-1}} \tag{8}$$

$$\varepsilon = \frac{r}{a\tau_e} \tag{9}$$

where a is the local sound speed, u_a is the speed of autoignition reaction front, τ_i is autoignition delay time, r is the radius of the hot spot, and τ_e is the excitation time. Specifically, τ_e is defined as the time interval between 5% and maximum heat release rate. $\partial \tau_i / \partial r$ is evaluated along the direction of autoignition front propagation. The hot spot radius is adopted according to the distribution of temperature and OH mass fraction before autoignition. The ignition delay time is calculated with the transient thermodynamic state and species concentration before autoignition. As shown in Fig. 18, the simulations with autoignition in section 3 are identified in Bradley's diagram except case 9. The autoignition takes place at the instant when the pressure waves reflect on the wall in case 9 as discussed above, and then it develops into a detonation wave immediately, before which an obvious temperature gradient is not observed. The detonation seems to be initiated directly in case 9 and thus it is not appropriate to identify it in Bradley's diagram since the latter is based on the reactivity gradient theory. This can be further confirmed by Fig. 10 and Fig. 13. From Fig. 13, it can be observed that the end-gas in case 9 goes through a much stronger constant volume combustion process than the other two cases at the same initial temperature, and this combustion process is extremely similar to that in case 6 as shown in Fig. 10. The strong constant volume combustion in

case 6 is in fact caused by the passage of the spherical detonation wave induced by the autoignition at the right upper corner. Therefore, the end-gas in case 9 should go through a detonation combustion process as well but the detonation is initiated directly by the autoignition.

Back to Fig. 18, it is observed that the locations of these cases in Bradley's diagram basically give a reasonable transition of the autoignition propagation modes, which agrees well with the observations in the simulations, although case 8 is located at below but extremely close to the lower limit of developing detonation regime. As mentioned above, Bradley's diagram is based on the reactivity gradient theory, and thus the autoignition propagation mode transition among different cases here should be as a result of the inhomogeneity induced by pressure waves. In previous studies, in fact, Terashima et al. [29] have proposed that the weak pressure wave can cause weak inhomogeneity, causing the autoignition to occur in the end-gas simultaneously, while the stronger one can induce the enhanced inhomogeneity which can lead to the detonation development. This is mostly consistent with the present results. However, the current studies further indicate that the effects of pressure wave on autoignition propagation modes should be considered along with the initial reactivity (initial temperature here) of the mixture. To be specific, when the pressure wave is weaker, there is only thermal explosion occurrence in the end-gas if the initial temperature is lower, like in case 4, whereas the localized thermal explosion may further develop into a detonation wave if the initial temperature is higher, like in case 7, because more fresh mixture is left at the moment of autoignition occurrence. When the pressure wave is stronger, only deflagration may be developed because of the larger reactivity gradient, if the initial temperature is lower, like in case 3, whereas the detonation can be initiated directly thanks to the higher reactivity of the mixture, if the initial temperature is much higher, like in case 9. Moreover, the results also show the autoignition propagation modes directly dominate the intensity of pressure oscillation in the chamber. The peak pressure in all cases are summarized in Table 1 and it is showed that the peak pressures in the cases with detonation development all reach up to hundreds of atmospheres, which is consistent with super-knock conditions in real engines, much higher than the case with thermal explosion.
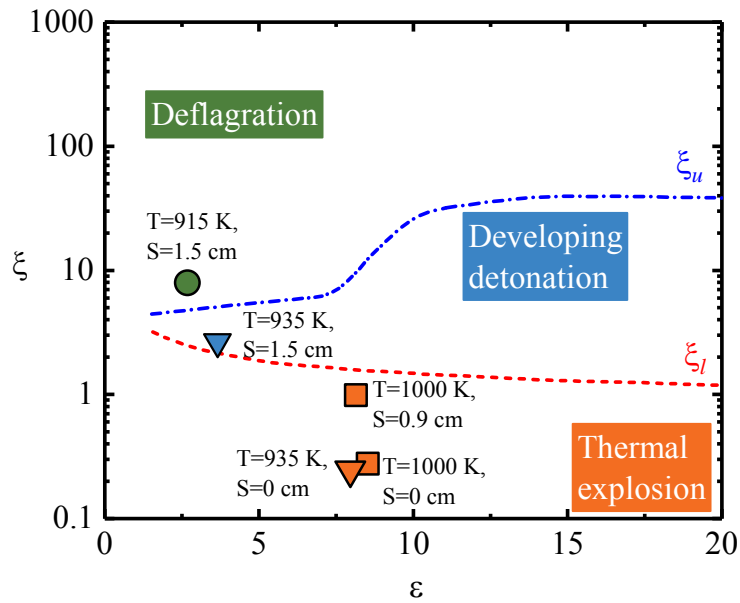
Fig. 18 Bradley's diagram

5. Conclusions

A set of 2D numerical simulations have been performed to identify end-gas combustion mode transition under different initial temperatures. The influence of pressure waves is emphasized in the present work. Flame propagation of stoichiometric hydrogen/air mixture in closed chambers with and without obstacles are discussed. When there are no obstacles, the flame propagates at a nearly constant mean speed along with slight oscillation, whereas with obstacles, the flame rapidly accelerates and dramatic oscillation of flame speed appears when the flame passes the obstacles. In addition, the evolution of flame speed with $S = 0.9$ cm can be divided into three stages. In the first stages, the flame accelerates because of obstacle disturbance. In the second stage, the flame has passed the last obstacle and keeps a nearly constant propagation speed. In the third stage, the flame accelerates again due to the flame surface area increase.

Different autoignition transition modes, including one transition from no autoignition to autoignition, two transitions of autoignition to no autoignition and no autoignition to autoignition again, and zero transition of autoignition invariably, are observed with increase of the initial temperature. The idealized physical model, with the Mach number of the pressure wave as the link between the flame propagation duration and ignition delay time of the end-gas, gives a reasonable description for these three autoignition transition modes. Evolutions of three transition limits, Ma_0, Ma_1, Ma_2 are identified. At the low temperature zone, Ma_0 shifts to a smaller Mach number with

increase of the initial temperature. At the moderate temperature zone, Ma_1 shifts to a larger Mach number, while Ma_2 shifts to a smaller Mach number as temperature increases, which makes the no autoignition zone disappears and autoignition occurs all the time at the high temperature zone. It is shown that autoignition can be suppressed by the elevated flame speed when the pressure wave is weak, while it cannot be prevented intrinsically if the temperature of end-gas is higher or the pressure wave is strong enough. There seems to exist a critical state that once the reactivity of the mixture is reached, it accelerates the reaction progress spontaneously until the autoignition occurs.

The autoignition propagation modes, including deflagration, developing detonation and thermal explosion are classified by Bradley's diagram. These different autoignition propagation modes arise from the combination effects of the initial reactivity and inhomogeneity induced by pressure waves. The results also show that there are three types of end-gas autoignition-induced detonation formation in the confined space: 1) detonation initiated directly by the pressure wave generated from the flame propagation (case 9); 2) detonation initiated directly by the pressure wave generated from other hot-spot autoignition (case 3); 3) autoignition to detonation transition based on the reactivity gradient theory (case 6 and case 8). In addition, flow particles are tracked to identify the end-gas combustion modes, and constant pressure combustion mode, constant volume combustion mode and the mode between them corresponds to the autoignition propagation modes of deflagration, developing detonation and thermal explosion, respectively.

Acknowledgments

Reference

[1] R.D. Reitz, G. Duraisamy, Prog. Energy Combust. 46 (2015) 12-71.
[2] J.E. Dec, Proc. Combust. Inst. 32 (2009) 2727-2742.
[3] Z. Wang, H. Liu, R.D. Reitz, Prog. Energy Combust. 61 (2017) 78-112.
[4] J. Rudloff, J.M. Zaccardi, S. Richard, J.M. Anderlohr, Proc. Combust. Inst. 34 (2013) 2959-2967.
[5] Y.B. Zeldovich, Combust. Flame 39 (1980) 211-214.

[6] L. Bates, D. Bradley, G. Paczko, N. Peters, Combust. Flame 166 (2016) 80-85.

[7] D. Bradley, G.T. Kalghatgi, Combust. Flame 156 (2009) 2307-2318.

[8] X.J. Gu, D.R. Emerson, D. Bradley, Combust. Flame 133 (2003) 63-74.

[9] P. Dai, Z. Chen, X. Gan, Combust. Flame 201 (2019) 208-214.

[10] J.F. Griffiths, B. Whitaker, Combust. Flame 131 (2002) 386-399.

[11] J. Pan, S. Dong, H. Wei, T. Li, G. Shu, L. Zhou, Combust. Flame 205 (2019) 269-277.

[12] P. Dai, C. Qi, Z. Chen, Proc. Combust. Inst. 36 (2017) 3643-3650.

[13] T. Zhang, W. Sun, L. Wang, Y. Ju, Combust. Flame 200 (2019) 342-353.

[14] M. Pöschl, T. Sattelmayer, Combust. Flame 153 (2008) 562-573.

[15] J. Cho, H.H. Song, Proc. Combust. Inst. 37 (2019) 4911-4919.

[16] M.A. Liberman, A.D. Kiverin, M.F. Ivanov, Physical review. E, Statistical, nonlinear, and soft matter physics 85 (2012) 056312.

[17] P. Dai, Z. Chen, S. Chen, Y. Ju, Proc. Combust. Inst. 35 (2015) 3045-3052.

[18] T. Zhang, W. Sun, Y. Ju, Proc. Combust. Inst. 36 (2017) 1539-1547.

[19] M.A. Liberman, M.F. Ivanov, O.E. Peil, D.M. Valiev, L.E. Eriksson, Combust. Sci. Technol. 177 (2004) 151-182.

[20] A. Robert, S. Richard, O. Colin, T. Poinsot, Combust. Flame 162 (2015) 2788-2807.

[21] Z. Wang, Y. Qi, X. He, J. Wang, S. Shuai, C.K. Law, Fuel 144 (2015) 222-227.

[22] H. Wei, D. Gao, L. Zhou, D. Feng, R. Chen, Combust. Flame 178 (2017) 277-285.

[23] L. Zhou, D. Gao, J. Zhao, H. Wei, X. Zhang, Z. Xu, R. Chen, Combust. Flame 191 (2018) 453-467.

[24] H. Wei, J. Zhao, X. Zhang, J. Pan, J. Hua, L. Zhou, Combust. Flame 204 (2019) 137-141.

[25] H. Wei, J. Zhao, L. Zhou, D. Gao, Z. Xu, Combust. Flame 186 (2017) 247-262.

[26] H. Wei, X. Zhang, H. Zeng, R. Deiterding, J. Pan, L. Zhou, Phys. Fluids 31 (2019); doi: 10.1063/1.5099456

[27] J. Pan, H. Wei, G. Shu, R. Chen, Combust. Flame 185 (2017) 63-74.

[28] H. Terashima, M. Koshi, Combust. Flame 162 (2015) 1944-1956.

[29] H. Terashima, A. Matsugi, M. Koshi, Combust. Flame 203 (2019) 204-216.

[30] J.C.Livengood, P.C.Wu, Proc. Combust. Inst. 5 (1955) 347-356.

[31] H. Yu, C. Qi, Z. Chen, Proc. Combust. Inst. 36 (2017) 3533-3541.

[32] L. Chen, H. Wei, C. Chen, D. Feng, L. Zhou, J. Pan, Energy 166 (2019) 318-325.

[33] CHEMKIN-PRO 10131, Reaction Design: San Diego, 2013.

[34] J. Li, Z. Zhao, A. Kazakov, F.L. Dryer, Int. J. Chem. Kinet. 36 (2004) 566-575.

[35] V.N. Gamezo, E.S. Oran, AIAA J. 44 (2006) 329-336.

[36] J.D. Ott, E.S. Oran, J.D. Anderson, AIAA J. 41 (2003) 1391-1396.

[37] M.-h. Wu, M.P. Burke, S.F. Son, R.A. Yetter, Proc. Combust. Inst. 31 (2007) 2429-2436.

[38] R. Deiterding, J. Combust. 2011 (2011) 1-18.

[39] R. Deiterding, Computers & Structures 87 (2009) 769-783.

[40] R. Deiterding, Parallel adaptive simulation of multi-dimensional detonation structures, Brandenburgische Technische Universität Cottbus, Cottbus, 2003.

[41] P.N. Brown, G.D. Byrne, A.C. Hindmarsh, J. Sci. Stat. Comput. 10 (1989) 1038-1051.

[42] R. Kee, F. Rupley, J. Miller, Chemkin-II: a Fortran chemical kinetics package for the analysis of gas-phase chemical kinetics, Sandia National Laboratories, Livermore, Calif, USA, 1989.

[43] X. Cai, R. Deiterding, J. Liang, Y. Mahmoudi, Proc. Combust. Inst. 36 (2017) 2725-2733.

[44] X. Cai, J. Liang, R. Deiterding, Y. Mahmoudi, M. Sun, Combust. Flame 190 (2018) 201-215.

[45] X. Cai, R. Deiterding, J. Liang, M. Sun, Y. Mahmoudi, J. Fluid Mech. 836 (2017) 324-351.

[46] H. Peng, Y. Huang, R. Deiterding, Z. Luan, F. Xing, Y. You, Combust. Flame 198 (2018) 69-80.

[47] Y. Wang, W. Han, R. Deiterding, Z. Chen, Phys. Rev. Fluids 3 (2018).

[48] H. Xiao, R.W. Houim, E.S. Oran, Proc. Combust. Inst. 36 (2017) 1577-1583.

[49] V.N. Gamezo, T. Ogawa, E.S. Oran, Combust. Flame 155 (2008) 302-315.

[50] C. Johansen, G. Ciccarelli, Combust. Flame 156 (2009) 405-416.

[51] D. Valiev, V. Bychkov, V.y. Akkerman, C.K. Law, L.-E. Eriksson, Combust. Flame 157 (2010) 1012-1021.

[52] D. Bradley, M. Lawes, K. Liu, Combust. Flame 154 (2008) 96-108.

[53] Q. Chen, Theory and experiment of the flow in shock tube, The China Science and Technology University Press, Hefei, 1979.

[54] Y. Qi, Y. Wang, Y. Li, J. Wang, X. He, Z. Wang, Combust. Flame 205 (2019) 378-388.